Article

Moiré collective vibrations in atomically thin van der Waals superlattices

Lijia Li [1] ✉, Jiajun Chen[1], Laigui Hu [1], Zhijun Qiu[1], Zhuo Zou[1], Ran Liu [1], Lirong Zheng [1] ✉ & Chunxiao Cong [1,2] ✉

Collective vibration is pivotal for materials' thermal, electrical, phase transition and topological properties. Lately, the rising of moiré superlattices, characterized by overarching periodicity of moiré pattern, generates highly tunable interfacial structures that manipulate collective excitations in material at the atomic scale. Here, we experimentally demonstrate moiré collective vibrations, the mechanical counterparts of moiré excitons, at heterointerfaces of twisted tungsten diselenide/tungsten disulfide heterobilayers. Using helicity-resolved inelastic Raman scattering, we find chiral interfacial phonons carrying angular momentum analogous to that of chiral bulk phonons in quartz, enabling unprecedented spectral resolution of rich vibrational modes at heterointerface in a few atomic layers. Upon mutual torsion of heterobilayers, we observe terahertz interlayer vibrations proportional to moiré periodicity as a periodic function of rotation angles, demonstrating moiré-tuned interlayer modes which couple to Coulomb-bound electron-hole pairs in interlayer moiré excitons. In low-angle strong coupling regime, interlayer dynamics exhibit a distinct long-lived breathing mode with zero angular momentum and pronounced high energy, highlighting phonon-hybridization character wherein intralayer breathing vibrations are folded into moiré mini-Brillouin zone by spatial periodicity and hybridize with interlayer vibrations. Our findings establish moiré collective vibrations as candidates for exploitation in energy-efficient thermal management, strongly correlated electrical engineering, and new emergent topological phononics.

Collective vibration dynamics in solids fundamentally govern many properties ranging from the thermal and electrical transport and superconductivity to topological states and phase transition[1–3]. On the practical side, the development of advanced technologies, such as transistors, solar cells, mechanical quantum computing and thermoelectrics, requires efficient vibrational engineering of materials[4–6]. As the length scales of materials decrease to nanometer sizes, the heterogeneities related to interfaces are of particular interest and become almost as important as the surrounding materials. In contrast to the measured and calculated collective excitations in bulk crystalline

materials[7,8], phonons remain poorly understood at atomic-scale interfaces in nanomaterials[5,9,10], despite the increasing prevalence of designer nanomaterials and the assembly of nanometric components into devices[11,12]. Although it is commonly accepted that intrinsic phonons change near boundaries[13,14], the intricate interfacial vibration and the vibration-material interaction subjected to heterointerfaces, such as superlattices[15–17] and other intergranular and interphase boundaries[18–20], remains largely unexplored.

Moiré superlattices are formed by stacking two layers of two-dimensional (2D) materials with a relative twist angle, which

[1]School of Information Science and Technology, Fudan University, Shanghai, PR China. [2]Yiwu Research Institute of Fudan University, Yiwu, Zhejiang, PR China. ✉e-mail: lilj21@m.fudan.edu.cn; lrzheng@fudan.edu.cn; cxcong@fudan.edu.cn

introduces an additional periodic structure landscape. The rigid twisted superlattice commonly undergoes a self-organized lattice reconstruction to reduce the stacking energy at van der Waals (vdW) interfaces[21–23]. The resulting superlattices have recently emerged as an intriguing platform to engineer vibrational[21,24] and electronic structures[25,26] within the material, leading to changes in the electron-phonon coupling ($e–ph$, fermion–boson)[27,28] and to the observation of diverse strong correlation phenomena[12]. For example, a wealth of correlation phenomena ranging from correlated Mott–Wigner states to the quantum anomalous Hall effect to superconductivity has been observed both in magic-angle-twisted bilayer and trilayer graphene[12,29–31] and in twisted bilayers of transition metal dichalcogenides (TMDCs)[32–37]. These twisted moiré superlattices are new material systems, in which interface localized vibration structures and phonon–material interaction related to the emerging moiré physical phenomena are highly desirable to be fully understood.

Despite their importance, quantitative studies, especially experimental ones, of phonons in moiré superlattices have remained prohibitively difficult. The major challenge is that they appear with both degenerate energy levels[38] and recently verified angular momenta from the phononic chirality[7,8], imposing stringent technical requirements, including high sensitivity, angular momentum transfer and ultrahigh energy resolution. Recent advances in inelastic X-ray scattering techniques are successful in bulk chiral vibrational state measurements with angular momentum transfer[7], but their sensitivity is insufficient for nanostructures[39]. Reflection electron energy-loss spectroscopy (EELS) can determine surface phonons[40,41], but their non-angular momentum selecting geometry makes phonon angular momentum measurements impossible. The TMDCs reportedly produced strong phonon-exciton coupling, enabling highly sensitive detection of phonons[42]. Their heterostructure generates particularly strong interlayer phonon-matter interaction wherein electron and hole constituents of interlayer exciton reside in opposite vibrating layers with a large binding energy of hundreds of milli-electron volts[33,43]. Hence, an experimental platform enabling both high angular momentum and energy resolutions of interfacial collective vibrations at the same time is vital for deepening understanding of moiré-induced phonon and phonon-material interaction at heterointerfaces.

In this study, we quantitatively measured the tunable collective vibrations from the moiré heterostructures composed of TMDC monolayers of tungsten disulfide (WS$_2$) and tungsten diselenide (WSe$_2$) with a full torsion angle range from zero to sixty degrees. We found interfacial phonons carrying angular momentum from the rotational symmetry of interface using inelastic Raman scattering with helical incident photons, in analogy with the recently identified bulk phonon chirality in quartz and rare-earth halides[7,8]. This identification of vibrational angular momentum at an interface can be extended for the solid interfaces with discrete spatial symmetry[44]. The selection rules from the angular momentum conservation enable us to study the interfacial vibrational states in unprecedented resolution[45], without relying on device energy resolution that is possibly hampered by energy degeneracy. The interlayer breathing vibration we observed oscillates at terahertz (THz) frequencies elegantly proportional to the moiré wavelength as a periodic function of the mutual torsion angle, showing tunable interlayer vibrations enforced by moiré potential. From the prominent redshifts of in-plane modes in the overall angle range, we deduced the deformation of WS$_2$ layer that agrees with the energy-favorable lattice relaxation driven by the interlayer coupling[26]. As the rotation approaches the appealing "magic" small angles, unconventional hybrid interlayer breathing modes occur with long lifetime, zero angular momentum and record-high energy above 3.8 meV, indicative of moiré interlayer phonon–phonon coupling ($ph–ph$, boson–boson)[29–37]. The splitting intralayer vibrations in this range suggest the self-organized symmetry-breaking lattice reconstruction, in the same league as the spontaneous reconstruction in the low-angle graphene bilayers[24]. Our results establish moiré collective vibrations as candidates to explore the phonon-related effects, such as energy-efficient interfacial thermal management[4,46], spin-phonon coupling[1,8,43], strongly correlated electrical engineering[47], as well as the topological phononics[48–51].

Results

Chiral collective dynamics at vdW interface

We measured the interfacial collective dynamics in prototypical moiré heterostructure of WSe$_2$/WS$_2$ by using helicity-resolved Raman scattering spectroscopy. WSe$_2$/WS$_2$ heterostructures were fabricated using single-layer (1 L) WSe$_2$ and 1 L WS$_2$ grown by chemical vapor deposition (CVD). The relative twist angle between the two layers was determined using polarization-dependent second-harmonic generation (SHG) measurements (Supplementary Fig. 1). The optical setup for helicity-resolved Raman spectroscopy is illustrated in Fig. 1a (Details in Supplementary Fig. 2). The optical image of a WSe$_2$/WS$_2$ heterostructure with a twist angle of 31.5° is shown in Fig. 1b. When the helicity of the scattered light (σ_s) matches that of the incident light (σ_i), denoted as $(\sigma_s \sigma_i) = (\sigma+\sigma+)$, it is classified as helicity-conserved scattering. Conversely, when σ_s and σ_i are opposite, represented as ($\sigma+\sigma-$), it corresponds to helicity-changed scattering. To evaluate the stability of the superlattice under the incident laser exposure, we performed a time series of Raman spectra and no detectable shift of phonon modes before degradation occurs (Supplementary Fig. 3).

The WS$_2$ (WSe$_2$) monolayer has a hexagonal structure with one tungsten and two sulfur (selenium) atoms in its unit cell[26]. The vibrations of these atoms can combine to form collective vibrational modes (Fig. 1c, d), commonly described in terms of a quasiparticle known as a phonon. Figure 1d illustrates the two types of optical phonons at the Brillouin zone (BZ) center: one type involves the out-of-plane relative vibrations of the sulfur (selenium) atoms, denoted as A_{1g} mode, and the other type arises from in-plane opposite motions of two sulfur (selenium) atoms relative to the tungsten atom within the 2D plane, denoted as E_{2g} mode. The E_{2g} mode is doubly degenerate at the BZ center[52]. Note that the energy resolution is insufficient for the assignment of individual phonons in conventional unpolarized Raman measurements (the optical setup for unpolarized Raman spectroscopy is illustrated in Supplementary Fig. 2) because E_{2g} and A_{1g} mode of monolayer WSe$_2$ have almost the same energy (Supplementary Fig. 4)[52]. For WSe$_2$/WS$_2$ heterostructure, interlayer interactions, such as van der Waals force, lead to new optical phonon branches, including layer breathing (LB) mode due to out-of-plane relative vibrations between two monolayers (Fig. 1c, left) and the shear (S) mode owing to in-plane relative vibrations (Fig. 1c, right)[53]. These interlayer modes have relatively low energy reflecting that the interlayer interactions are much weaker than the covalent bonding within each monolayer.

Figure. 1e, f shows the representative helicity-resolved Raman spectra (dark-colored lines for $\sigma+\sigma+$, light-colored lines for $\sigma+\sigma-$) of WS$_2$ monolayer (red), WSe$_2$ monolayer (blue), and the twisted heterostructure (black). The measured spectra feature several polarization-resolved phonon modes divided into the low-frequency (Fig. 1e) and high-frequency ranges (Fig. 1f). In low-frequency range, the main spectral signatures of the heterostructure are the emergence of LB mode in helicity-conserved spectrum and S mode in helicity-changed spectrum. These two modes are convincing evidence that the strong interaction between the layers exists[53]. The moiré interlayer interaction has attracted increasing interest, exemplified by the prediction of strong interlayer coupling from the observation of Van Hove singularity (VHS) signatures using valley-resolved scanning tunneling spectroscopy (STS)[54]. We note that the small peaks related to WS$_2$ and WSe$_2$ monolayers (marked by the dashed lines in Supplementary Figs. S4 and S5; Supplementary Fig. S6 shows the Savitzky-Golay processing) are observed in many TMD materials, the origin of which remains unexplained. In the high-frequency range, the Raman spectra
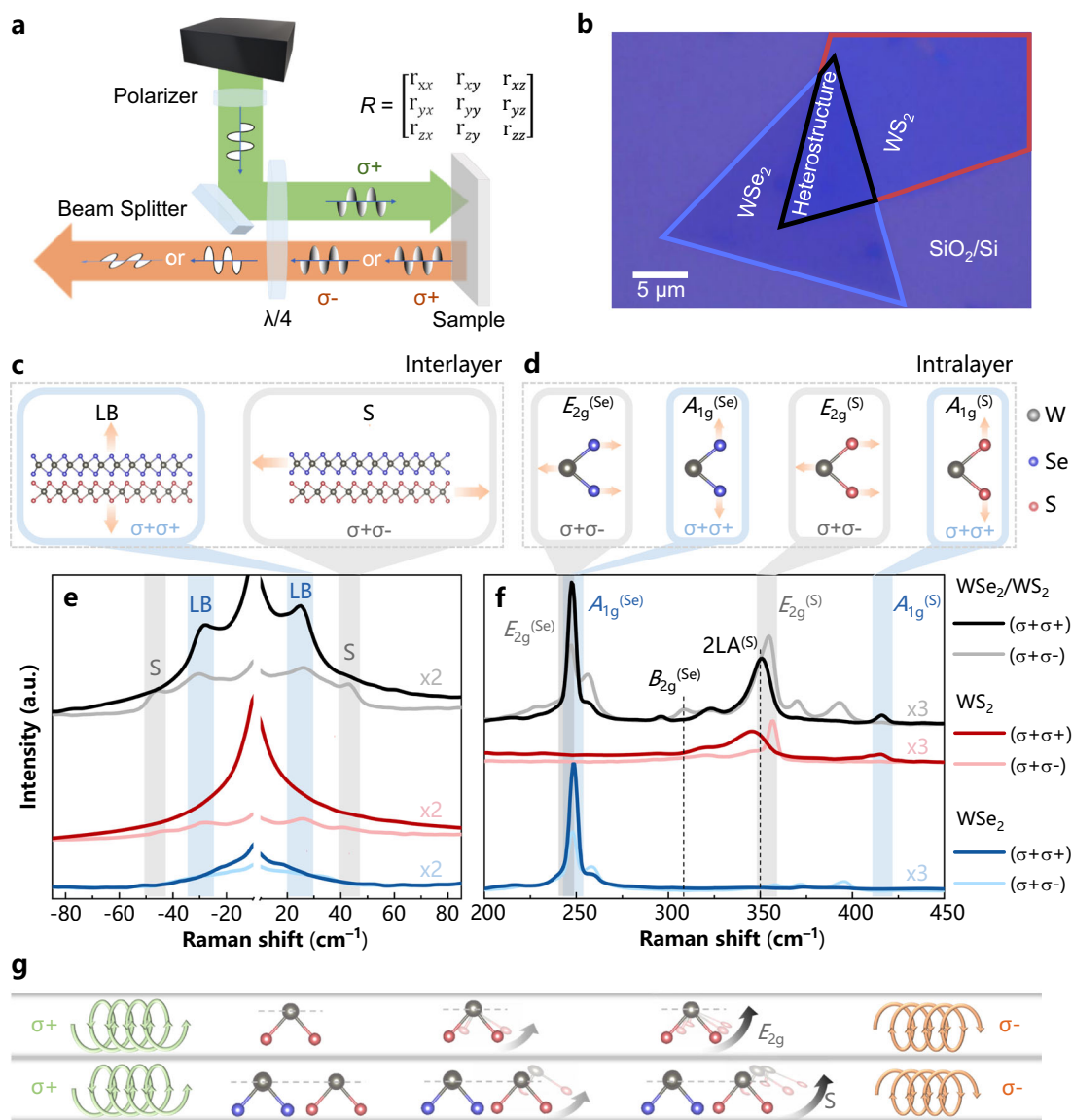
Fig. 1 | Chiral interfacial collective dynamics in WSe$_2$/WS$_2$ heterostructure.
a Schematic of experimental set-up for helicity-resolved Raman spectroscopy. The green (orange) path is for incident (scattered) light. **b** Optical microscope image of a typical WSe$_2$/WS$_2$ heterostructure sample. **c** Schematic illustration of atomic eigenvectors for interlayer breathing (LB) and shear (S) vibrational modes depicted by the orange arrows. The LB mode (S mode) corresponds to out-of-plane (in-plane) relative motions of the constituent layers. **d** Schematic illustration of atomic eigenvectors for E_{2g} and A_{1g} vibrational modes depicted by the orange arrows. The $E_{2g}^{(S)}$ ($E_{2g}^{(Se)}$) mode corresponds to in-plane relative motion between tungsten and sulfur (selenium) atoms in WS$_2$ (WSe$_2$); the $A_{1g}^{(S)}$ ($A_{1g}^{(Se)}$) mode corresponds to out-of-plane sulfur (selenium) atom vibrations. Representative low-frequency (**e**) and

high-frequency (**f**) helicity-resolved Raman spectra of the WSe$_2$/WS$_2$ hetero-structure (black) compared with monolayer WS$_2$ (red) and WSe$_2$ (blue), with helicity-conserved ($\sigma+\sigma+$) (dark color curves) and helicity-changed ($\sigma+\sigma-$) (light color curves) configurations, respectively. The spectra of helicity-changed ($\sigma+\sigma-$) configurations are scaled for clarity and the scale factors are shown on the edge of the panel. The $B_{2g}^{(Se)}$ and $2LA^{(S)}$ modes are indicated by dashed lines. The helicity-conserved LB and A_{1g} modes (indicated by blue shadow) are evidently dis-tinguished from the helicity-changed S and E_{2g} modes (indicated by gray shadow) by different helicity selection rules. **g** The angular momentum of incident photons is transferred to lattice vibrations (intralayer (up) and interlayer (down)) and the scattered photons have different circular polarization.

of the heterostructure are roughly a superposition of those of indivi-dual WS$_2$ and WSe$_2$ monolayers with subtle energy shifts. The A_{1g} modes of WS$_2$ and WSe$_2$ monolayer are observed in helicity-conserved polarization, while the E_{2g} modes of WS$_2$ and WSe$_2$ monolayer are detected in helicity-changed polarization. The helicity-resolved Raman scattering evidently resolves the A_{1g} and E_{2g} modes of WSe$_2$ despite their nearly degenerate energies and matches well with the calculated phonon energy at BZ center (Supplementary Fig. 7). Remarkably, the intensity of high-frequency modes is expected to be sensitive to the interlayer charge transfer[52,55,56], further computational studies would be required to clearly manifest the underlying physics.

We then extract the angular momentum of phonons at vdW interfaces from these helicity selection scenarios, by considering the symmetry requirement and angular momentum conservation. Monolayer WS$_2$ and WSe$_2$ are invariant under the 12 symmetry operations in the D_{3h} point group (Supplementary Fig. 8). The zone center optical phonons transform according to the irreducible representations of the group[57]. For the phonon scattering processes, Raman selection rules determine the Raman intensity I_O for off-resonance scenarios as $I_O = A\,|\langle\tilde{\sigma}_s\,|\,R\,|\,\tilde{\sigma}_i\rangle|^2$, where A is a constant, R is the Raman tensor of the corresponding mode, and $\tilde{\sigma}_s$ and $\tilde{\sigma}_i$ repre-sent the electric field vectors of scattered and incident photons,

respectively. For A_{1g} modes, the Raman tensor is given by $\begin{bmatrix} a & 0 & 0 \\ 0 & a & 0 \\ 0 & 0 & b \end{bmatrix}$, where a and b represent the elements in the Raman tensors in Cartesian coordinates. For same circular-polarization incident and scattering light, $\sigma_i = \sigma_s = 1/\sqrt{2} \begin{bmatrix} 1 \\ -i \\ 0 \end{bmatrix}$, $\sigma_s^\dagger |R| \sigma_i = a$. On the contrary, if $\tilde{\sigma}_s$ and $\tilde{\sigma}_i$ have opposite helicity, $\sigma_s^\dagger |R| \sigma_i = 0$. This symmetry consideration is consistent with Fig. 1f where the photons scattered by A_{1g} phonons with zero pseudoangular momentum (PAM)[58] have the same angular momentum as that of the incident photons owing to angular momentum conservation. For the E_{2g} mode, the Raman tensor is $\begin{bmatrix} 0 & c & 0 \\ c & 0 & 0 \\ 0 & 0 & 0 \end{bmatrix}$, where c represents the element in the Raman tensors in Cartesian coordinates. Similar calculations show that $\sigma_s^\dagger |R| \sigma_i$ is zero (nonzero) for the same (opposite) σ_i and σ_s angular momentum. This agrees with the selective helicity in Fig. 1f where the photons scattered by E_{2g} phonons with ±1 PAM reverse the angular momentum due to angular momentum conservation and are absent in the $(\sigma + \sigma +)$ configuration[58]. The helicity selection rules are anticipated to apply as well to the interlayer shear and breathing modes in few-layer TMDCs (Supplementary Note. 1 has symmetry considerations). The breathing mode preserves photon angular momentum while the shear mode reverses photon angular momentum. Such selection rules demonstrate unambiguously that circularly polarized chiral photons couple to chiral phonons due to the conservation of angular momenta in Raman scattering process (Supplementary Note. 2). Figure 1g shows conceptually how angular momentum is transferred from circularly polarized photons to the lattice of the heterostructure to launch chiral vibrations when the incident and scattered photons have different circular polarization. This process can provide insight into the phonon chirality and enables the detailed interrogation of moiré-induced lattice dynamic behavior at the interface.

Moiré-tunable interlayer vibrations

We prove that the interfacial vibration energy, and hence the interlayer coupling, is moiré-tunable by the mutual torsion of vdW heterointerface. Figure 2a shows the helicity-resolved low-frequency phonon modes measured from WSe₂/WS₂ heterostructures in the entire twist angle range from 0° to 60°. The low-frequency modes provide a sensitive probe of the interlayer interactions between the layers[53]. With twist angles starting from nearly 0°, the interlayer breathing mode shows a significant twist-angle dependence. A continuous blueshift of the breathing mode up to 25.33 cm⁻¹ (corresponding to 0.76 THz) with increasing twist angle is observed in the heterostructure up to twist angles of around 30°, beyond which the breathing mode frequency drops significantly. The variations of mutual torsion angle are expected to modulate interlayer hybridization of electronic states[43] and moiré potential confined interlayer excitons[42,56], thereby affecting the interlayer interactions (Fig. 2b). To disentangle the possible twist-angle dependent moiré configuration effects on interface dynamics in the twisted heterostructure, we analyze the moiré superlattice structure. The periodicity of the moiré supercells (Fig. 2c, top), also known as the moiré wavelength, λ_m, and the size of the mini-Brillouin zone of the moiré superlattice (Fig. 2c, bottom) are both highly dependent on twist angle (θ). The unit cell for the moiré pattern with lattice vector λ_m can be defined, and its lattice constant varies with the twist angle according to $\lambda_m = (1-\delta)a/\sqrt{2(1-\delta)(1-\cos\theta)+\delta^2}$, where a is the lattice constant of WSe₂, δ is the lattice mismatch between WSe₂ (3.18 Å) and WS₂ (3.32 Å)[59]. In the reciprocal space, the primitive vector of the moiré superlattice ($|\mathbf{g}|$) is given by $|\mathbf{g}| = \frac{2\pi}{a} \sqrt{\left(1 - \frac{\cos\theta}{1+\delta}\right)^2 + \left(\frac{\sin\theta}{1+\delta}\right)^2}$

(Supplementary Note. 3). The moiré potential acting on the WS₂ electrons is entirely electrostatic in nature, arising from the interlayer charge transfer driven by the broken inversion symmetry of the structure. Intralayer moiré phonons are activated by the moiré potential and arise as satellite Raman peaks from the heterostructure region (Supplementary Fig. 9). Figure 2d summarizes the periodic twist-angle dependence of the breathing mode frequencies (blue circles) extracted from the Raman spectra of Fig. 2a (Supplementary Fig. 10 shows the twist-angle dependence of shear modes). The phononic dependence on twist angle corresponds with the calculated moiré period (depicted by the gray dashed line), exhibiting slight deviations near 0° and 60°. This suggests that the moiré-tunable interfacial vibrations are enforced by the combined effects of hybridized electronic states and moiré interlayer excitons[42,43]. The interlayer exciton density does not play a dominant role in shifting phonon frequencies (Supplementary Fig. 11), suggesting that hybridized electronic states are the primary factor influencing the twist angle-dependent phonon energies. The trend of low-frequency band in unpolarized Raman spectra shows the similar twist-angle dependence in consistent with the observation in circularly-polarized Raman spectra (Supplementary Fig. 12). The difference of Raman scattering with right-circularly polarized and left-circularly polarized light is negligible (Supplementary Fig. 13), suggesting that the influence of electronic transition pathways on the polarized Raman spectrum is not significant.

Moiré-tunable intralayer vibrations

A detailed analysis of the twist-angle-dependent intralayer vibration validates the phonon-exciton coupling tunability at the vdW interface, as presented in Fig. 3a–d, (see Supplementary Fig. 14 for the corresponding unpolarized energy-degenerate phonon spectra). The maximum Raman intensity of WSe₂ is achieved with small moiré period, whereas intralayer vibrations in WS₂ exhibit maximum intensity with large moiré period, showing enhanced phonon-electron coupling driven by the interlayer charge transfer in low-angle regime[43]. The presence of interlayer coupling is expected to introduce lattice relaxation impact on high-frequency intralayer vibrations, which are sensitive to the variation of interatomic bonding strength[24]. The atomic relaxation of the WSe₂/WS₂ moiré superlattices is detected by ADF-STEM and low-loss STEM-EELS in recent works[26,60]. The atoms modulate their positions in favor of lattice commensuration and deviate from their equilibrium positions, leading to expected changes in interatomic vibrations. The peak position values extracted from the spectra are summarized in Fig. 3e. The frequency of A_{1g} and E_{2g} mode for WSe₂ vary slightly by approximately 1 cm⁻¹ with no monotonic dependence on the twist angle. However, the frequency of the E_{2g} and A_{1g} modes for WS₂ shows a clear dependence on the twist angle. At small twist angles, especially below 10°, the E_{2g} and A_{1g} modes of WS₂ manifest redshifts as the twist angle decreases. The E_{2g} mode exhibits a pronounced response in twisted heterostructures, displaced by up to approximately 4 cm⁻¹ in large moiré period region (~7 nm). Notably, all of the E_{2g} modes of WS₂ in heterostructure samples are slightly redshifted compared with that of the monolayer WS₂, even for larger twist angles. In few-layer TMDC, the redshift of the E_{2g} mode is usually associated with an increase in the number of layers[61] or the existence of in-plane strain[62]. The observation that the intralayer modes of WS₂ are affected more than those of WSe₂ can be attributed to the large difference in the shear deformation potential of WS₂ and WSe₂ (0.14 versus 0.10, respectively)[63], which results in the in-plane strain being mostly located in the WS₂ layer. A schematic of the moiré superlattice is shown in Fig. 3f, with three high-symmetry stacking configurations of AA (metal vertically stacks on chalcogens), B^{Se/W} (Bernal AB stacking with Se stacked on W), and B^{W/S} (Bernal AB stacking with W stacked on S). Because of steric effects, density functional theory
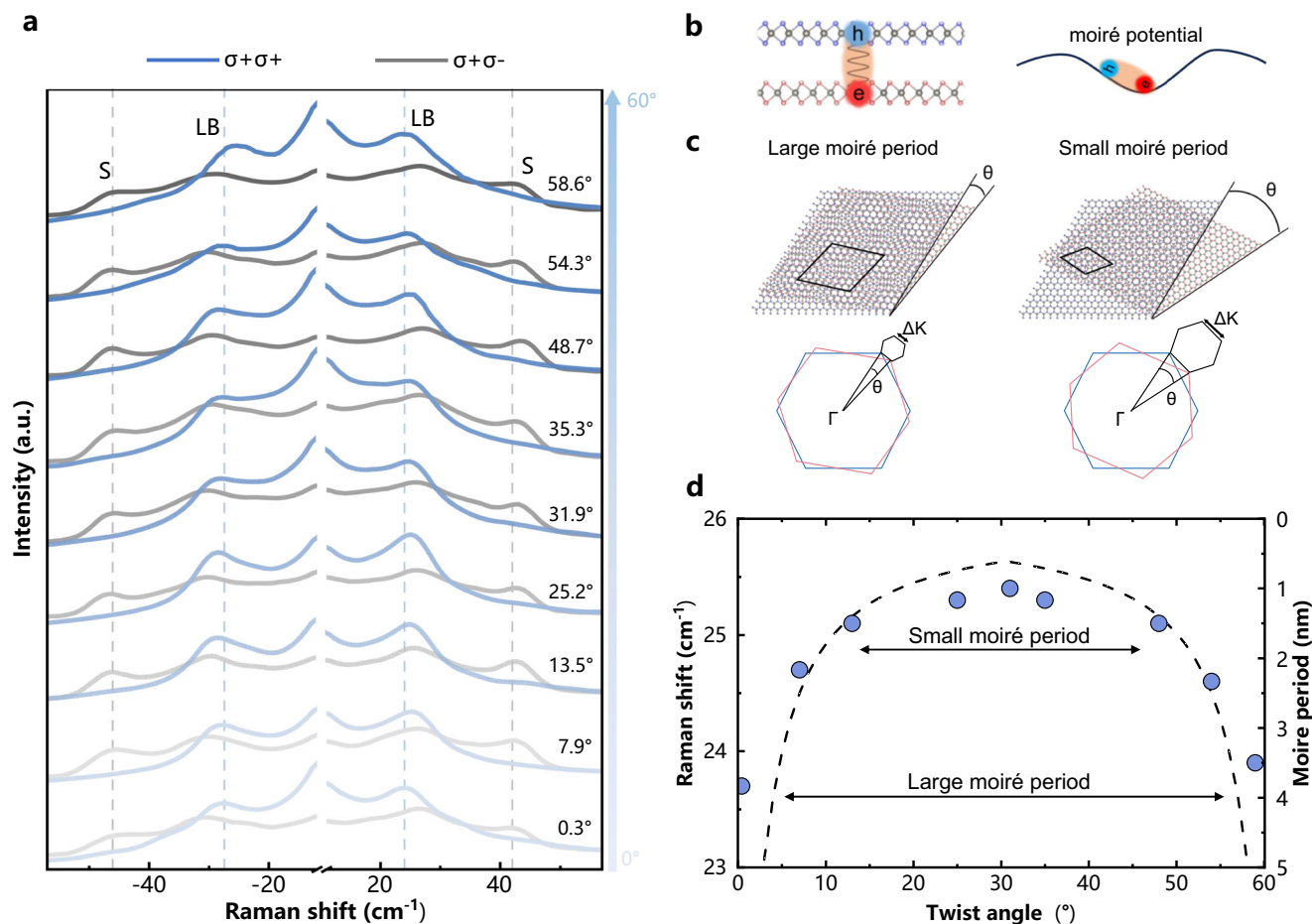
Fig. 2 | Moiré-tunable interlayer vibrations in the vdW heterostructure. a Low-frequency chiral Raman spectra of WSe$_2$/WS$_2$ moiré superlattice as a function of twist angle. The frequency of interlayer LB and S modes with nearly 0° twist angle is indicated by the blue and gray dashed lines, respectively. The spectra of helicity-changed ($\sigma + \sigma$-) configurations are scaled for clarity by a scale factor of 2. **b** Schematic of the interlayer LB phonon which couples strongly with IXs because the vibrational mode is directly modulated by the vertical Coulomb-bound electron-hole pair of exciton (left). Moiré-trapped excitons are localized and controlled by the potential wells (right). **c** Illustration of WSe$_2$/WS$_2$ moiré superlattice in real space (top panel) and mini-Brillouin zone generated from the difference between two wavevectors in reciprocal space (bottom panel). The WSe$_2$/WS$_2$ moiré super-lattice has a larger moiré period with twist angles close to 0° or 60° (left column) than that with twist angles close to 30° (right column). **d** The twist angle depen-dence of the LB mode frequency (blue circles). Errors from peak fitting are smaller than the diameter of the circles. The dashed curve shows the twist-angle depen-dence of the moiré period for reference.

calculations have predicted that stacking in the moiré superlattice affects the local energy landscape with the highest energy in AA stacking region[26]. The superlattice tends to increase the area of the interlayer-locked AB stacking regions due to its lower energy than AA stacking (Fig. 3g). As a result, the WS$_2$ layer becomes locally stretched at the AB stacking regions due to its smaller lattice constant com-pared with WSe$_2$, which is consistent with the shift observed in the E_{2g} modes of WS$_2$. The inhomogeneous strains lead to a spatial mod-ulation of the collective vibrations[52], electronic wavefunctions[64] and the phonon-exciton coupling due to spin-boson interaction between colocalized interlayer excitons and phonons[42,43]. However, a com-prehensive quantitative analysis necessitates further theoretical advancements to effectively account for the twist-angle-dependent electron-phonon coupling in these complex systems.

Moiré-induced hybrid phonons in strong coupling regime
We next discuss the interfacial dynamics in the strong coupling regime, namely the "magic twist angle" range. To verify the phononic recon-struction in this strong coupling regime, more heterostructures were fabricated and measured with twist angles ranging from ~0.3° to 7.9°. The measured spectra also feature the phonon modes divided into the low-frequency (Fig. 4a) and high-frequency ranges (Fig. 4b and Sup-plementary Fig. 15). The Raman spectra were smoothed using the

Savitzky–Golay algorithm (Supplementary Fig. 16). As the twist angle increases, the conventionally observed low-frequency LB mode blue-shifts slightly with the twist angle. (see Supplementary Fig. 17 for the corresponding unpolarized Raman spectra and Supplementary Fig. 18 for resolving the ambiguous splitting and energy-degenerate modes in unpolarized Raman spectra at 5.3°, 1.5° and 0.3°). Unexpectedly, in addition to the commonly observed low-frequency LB and S modes, we find that a new branch of the LB mode (denoted as LB$_{hyb}$) emerges at 31 cm^{-1}, carrying frequency of $\omega_{LB} \approx 0.93$ THz (ω_{LB}, LB-band frequency), an energy of $\hbar\omega_{LB} \approx 3.8$ meV ($\hbar$, reduced Planck constant) and zero angular momentum. The lifetime of LB$_{hyb}$ mode is $\tau = \hbar/\gamma \approx 0.86$ ps (γ, LB-band linewidth) under the assumption that the linewidth arises pri-marily from phonon decay. This mode exhibits a distinct polarization dependence with ($\sigma + \sigma +$) configuration and are absent in large-angle systems. The LB$_{hyb}$ blueshifts and reaches a maximum frequency and lifetime near the angle of 3.8°. As the twist angle further increases, LB$_{hyb}$ redshifts and disappears in sample with a 7.9° twist angle. Since strong coupling region only accounts for a fraction of the total sample area, the weak LB$_{hyb}$ is observed in our far-field measurements.

In this scenario, with the presence of periodic moiré pattern, a plausible explanation for the appearance of LB$_{hyb}$ modes is the pho-nonic hybridization between interlayer modes and the out-of-plane acoustic (ZA) modes folded into mini-Brillouin zone by moiré spatial
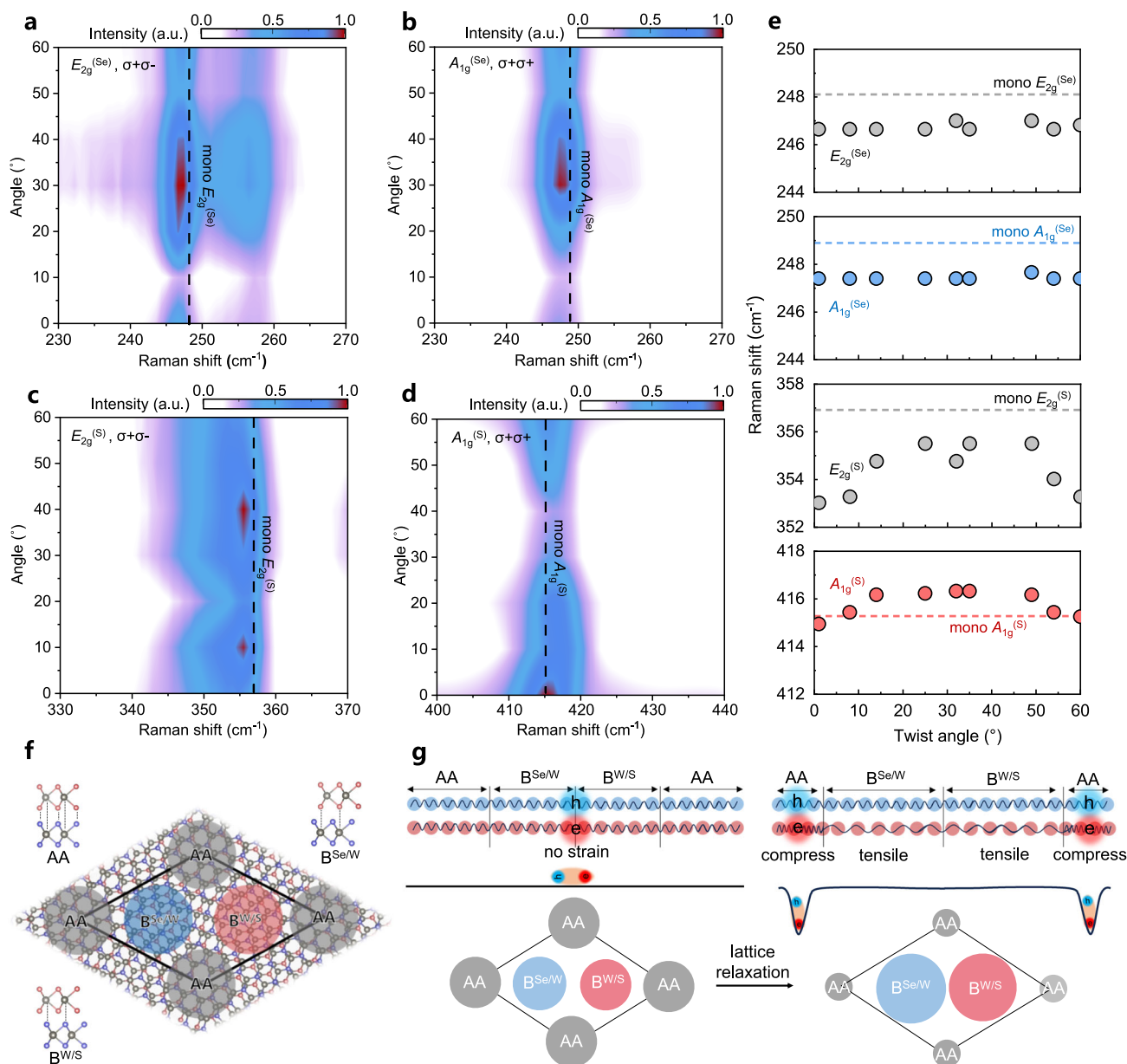
Fig. 3 | Correlation between the tunable intralayer vibrations and phonon-electron coupling in relaxed lattice. Color map of chirality-resolved Raman spectra of twisted WSe_2/WS_2 moiré superlattice from 200 to 450 cm^{-1} spectrum range highlighting in-plane and out-of-plane modes of WS_2 (**a**, **b**) and WSe_2 (**c**, **d**). The peak positions from monolayer WSe_2 and WS_2 are indicated by dashed lines for comparison. **e** Peak position as a function of the twist angle for the $E_{2g}^{(Se)}$, $A_{1g}^{(Se)}$, $E_{2g}^{(S)}$ and $A_{1g}^{(S)}$ modes. Errors from peak fitting are smaller than the diameter of the circles. The peak positions from monolayer WSe_2 and WS_2 are indicated by dashed lines for comparison. **f** Structural model of WSe_2/WS_2 moiré superlattice showing different stacking configurations in a moiré unit cell. **g** Schematic of the lattice relaxation process. The relaxation increases the area of the interlayer-locked AB stacking regions due to its lower energy (top), and the WS_2 layer becomes locally stretched at the AB stacking regions with the residual compressional strain localizes to the AA stacking region (bottom), where excitons are funneled into and localized by the strain-induced potential traps (middle).

periodicity (Fig. 4c, d and Supplementary Note 4). To aid the interpretation of spectral features, Supplementary Fig. 19 shows a comparison between the DFT-computed frequencies for monolayer WS_2 and WSe_2 phonon states with momenta **g**, which fold onto the moiré BZ center, as well as the frequencies of experimentally observed LB_{hyb} modes. We find the emergence of LB_{hyb} modes as the dispersive folded ZA modes approach the energy of the LB mode in the range $0.3° < \theta < 5.3°$. Within this range, the energy proximity of the ZA and LB modes appears to the coupling condition precisely. Clear signatures of lattice reconstruction in this regime are also found in the high-frequency E_{2g} mode. Although the high-frequency modes of WSe_2 are nearly independent of twist angle (Supplementary Fig. 15), the E_{2g}

mode of WS_2 evolves into a doublet E_{2g}^+ and E_{2g}^- at $0.3° < \theta < 5.3°$ (Fig. 4b), which provides evidence of high in-plane strain locally breaks the three-fold rotational symmetry of hexagonal unit cell (Supplementary Note 5). The reconstructed regime identified by helicity-resolved Raman spectra at $\theta < 5.3°$ agrees remarkably well with a recent STEM study performed on mechanically stacked twist bilayers[60]. At small angles, the real space supercell is very large, allowing significant lattice relaxation even though it is driven by weak van der Waals interactions between the layers and inhibited by strong in-plane bonding within each layer[26]. The dramatic atomic reconstruction of rigid lattice forms large triangular regions in which the energetically favorable $B^{Se/W}$ ($B^{W/S}$) stacking (or 3R stacking for $\theta = 0°$) are
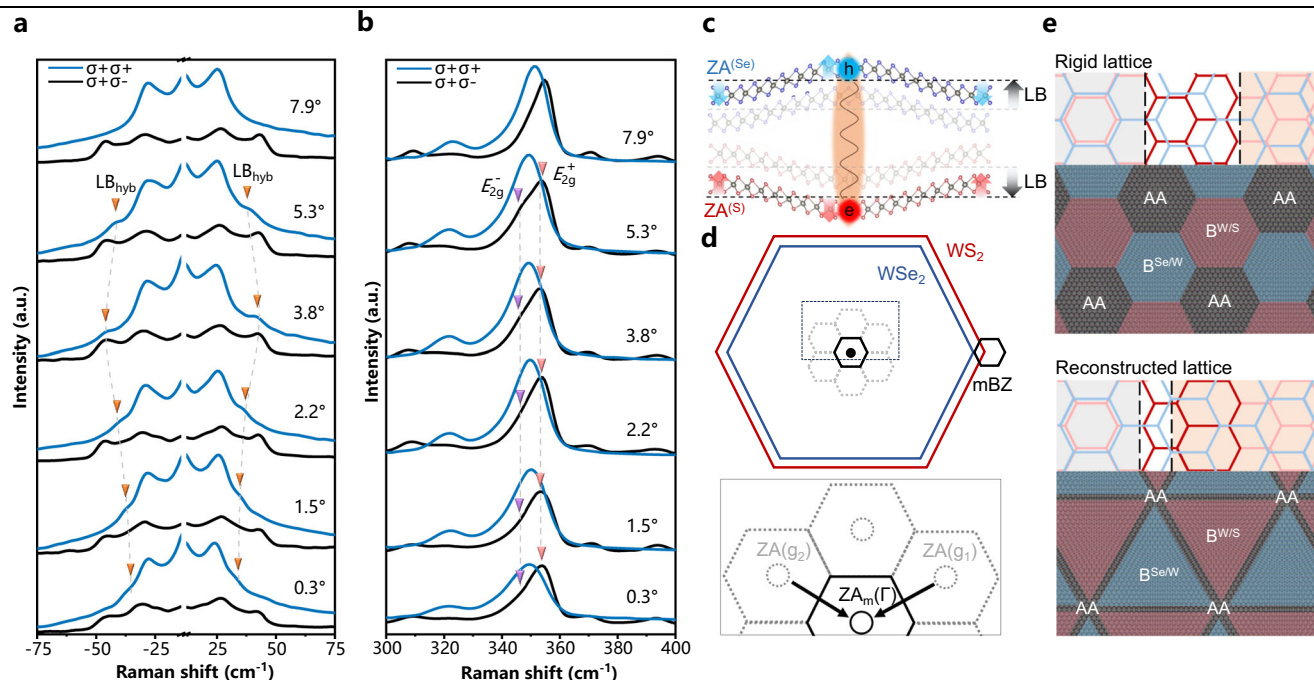
Fig. 4 | Hybrid moiré phonons in the strong coupling regime. a, b Emergence and evolution of hybridized interlayer LB_{hyb} mode and the two splitting intralayer E_{2g}^+ and E_{2g}^- modes of WS_2 in reconstruction regime ($\theta < 8°$). The spectra of helicity-changed ($\sigma + \sigma-$) configurations are scaled for clarity by a scale factor of 2 (**a**) and 3 (**b**), respectively. **c** Schematic of exciton-phonon coupling with the colocalization of the IX and the hybridization of LB and ZA phonons. **d** Moiré

Brillouin zone and the folded ZA phonon at the primitive moiré reciprocal vectors g_n ($n = 1, 2$) in WSe_2/WS_2 heterostructure with twist angles close to 0°. **e** Schematic illustration of the rigid and constructed moiré superlattice with twist angles close to 0°, with the symmetry-broken lattice in the intermediate region (white shade) between AA (gray shade) and AB (orange shade) stacking regions (exaggerated for clarity).

approached, as illustrated in Fig. 4e. Notably, our measurements report averaged strain under the laser spot. Future near-field experiments[40,65] combined with chirality-resolved nano-Raman may reveal the contribution of local variations of dynamics within a moiré supercell. However, reaching the spatial resolution for this regime where supercell size ranges from 8 nm (0°) to 2 nm (8°), would be very challenging. Such drastic changes in collective vibrations at low twist angles in chiral Raman spectra offer a simple and powerful spectroscopy technique to evaluate twist-angle disorder at moiré interface and to explore regions close to the magic angle where many-body interactions dominate over kinetic energy[12,66]. Given that future applications will involve diverse interfacial structures and increasingly large spectral data sets, it will be interesting to investigate whether machine-learning approaches could be used to develop general models that relate the structures of moiré superlattices to their lattice dynamics.

Discussion

In summary, we have experimentally demonstrated the existence of moiré-induced mechanical collective excitations that correspond to moiré excitons driven by spatial periodicity in WS_2/WSe_2 hetero-bilayers. The energy level and angular momentum of terahertz lattice vibrational modes localized at heterointerface are verified by symmetry requirement and angular momentum conservation using the helicity-resolved Raman scattering. We firmly established the moiré potential origin of the interfacial collective dynamic tunability, which correlates with the proximity-induced spin-boson coupling between interlayer excitons and phonons. In contrast to the previously studied interlayer vibrational modes, the emergence of hybridized interlayer breathing modes in magic-angle range are quantitatively interpreted as the phonon hybridization that includes the periodicity-folded phonons in moiré mini-Brillouin zone. All these features provide an essential basis for understanding moiré collective dynamics and would be helpful for further realizing designer phononic states and Bose-

Fermi interactions consisting of phonon condensate generated by the presence of moiré periodicity. For example, tailoring inter-facial moiré lattice dynamics could offer a new route to energy-efficient thermal conductance which is govern by terahertz phonons at room temperature, high-mobility electron transport which has orders-of-magnitude stronger electron-phonon coupling with interfacial vibrations than with bulk vibrations and exotic topological phononics.

Methods

Sample preparation
Monolayer crystals of WS_2 and WSe_2 were grown by CVD with a quartz tube (6 cm in diameter) under ambient pressure[67]. WO_3 (Alfa Aesar, 99.9%) was first deposited onto a silicon (Si) wafer coated with a 300 nm silicon oxide (SiO_2) layer as a W precursor through thermal evaporation. Another SiO_2/Si substrate was placed upside down above it. A quartz boat containing 200 mg of S (Se) powder (Aladdin, 99.99%) as S (Se) precursor was placed upstream of the furnace. For the WS_2 (WSe_2) monolayer, the growth temperature was 950 °C under a flow of Ar gas (100 s.c.c.m.) for 20 min. The furnace was cooled down to room temperature after growth.

For the fabrication of heterostructures, the CVD-grown monolayers were transferred by combining the wet and dry transfer methods[68]. A clean PDMS stamp was first placed on a glass slide. The SiO_2/Si substrate containing the as-grown CVD WSe_2 monolayers was brought in contact with the PDMS stamp. The deionized water droplets were injected at the perimeter of the substrate and penetrated into the $SiO_2/WSe_2/PDMS$ interface. After 10 min, the SiO_2/Si substrate was lifted and WSe_2 monolayers were transferred onto the PDMS stamp. The resulting samples were dried with a nitrogen gun. Finally, dry transfer of the WSe_2 monolayers from the PDMS stamp onto the top of the WS_2 samples was applied in a micromanipulator system. Thermal annealing at 90° for 30 min is performed for each transfer step.

Optical measurements

Raman measurements were performed using a confocal micro-Raman system (WITec Alpha 300 R) with a 532 nm continuous wavelength (CW) laser as the excitation source. A ×100 objective lens (Zeiss, 0.9 NA) was used to focus the laser beam onto the sample and to collect the scattered light (backscattering geometry). A grating with 1800 grooves per mm was used in the Raman measurements. For chiral Raman measurements, polarizers set the linear polarization of incident light and measured signals; a half-wave plate (Thorlabs) tunes the linear polarization of the pump; a quarter-wave plate (Thorlabs) with linear polarized light generates the circularly polarized light; and the polarizer and half-wave plate (Thorlabs) in front of the spectrometer analyze the scattered photon polarizations. For the SHG measurements, we use the same system with a 1064 nm picosecond laser for excitation.

Density functional theory calculations

The phonon dispersion of monolayer WS_2 and WSe_2 was calculated using the Quantum Espresso code[69] with the Phonopy package[70], making use of the norm-conserving pseudopotential within the local density approximation of Perdew–Zunger. The kinetic energy cutoff for charge density is 260 Ry. The first Brillouin zone is sampled with a $31 \times 31 \times 1$ Monkhorst–Pack grid. All of the atomic coordinates and lattice constants are optimized with the Broyden–Fletcher–Goldfarb–Shanno (BFGS) quasi-Newton algorithm until the Hellmann–Feynman force acting on each ion is less than 0.003 eV Å^{-1}. A vacuum spacing of 30 Å was used to avoid interactions between the layers.

Data analysis

Unsmoothed data without outlier removal were used to determine intensities and band positions. Outliers, generally caused by cosmic rays or charge buildup on the detector, were removed through subtraction and then the remaining data were interpolated across the spectrum. Raman spectra were smoothed using the Savitzky–Golay algorithm with 5 pt.

Data availability

The data generated in this study have been deposited in the Figshare (https://doi.org/10.6084/m9.figshare.28164446).

Code availability

The codes used for simulation and data plotting are available from the corresponding authors upon request.

References

1. Davies, C. S. et al. Phononic switching of magnetization by the ultrafast Barnett effect. *Nature* **628**, 540–544 (2024).
2. Girvin, S. M. & Yang, K. *Modern Condensed Matter Physics* (Cambridge University Press, 2019).
3. Masri, P. Surface and interface phonons and related topics. *Surf. Sci. Rep.* **9**, 293–369 (1988).
4. Yang, L. et al. Suppressed thermal transport in silicon nanoribbons by inhomogeneous strain. *Nature* **629**, 1021–1026 (2024).
5. Qiao, H. et al. Splitting phonons: building a platform for linear mechanical quantum computing. *Science* **380**, 1030–1033 (2023).
6. Giri, A. & Hopkins, P. E. A review of experimental and computational advances in thermal boundary conductance and nanoscale thermal transport across solid interfaces. *Adv. Funct. Mater.* **30**, 1903857 (2020).
7. Ueda, H. et al. Chiral phonons in quartz probed by X-rays. *Nature* **618**, 946–950 (2023).
8. Luo, J. et al. Large effective magnetic fields from chiral phonons in rare-earth halides. *Science* **382**, 698–702 (2023).
9. Kambhampati, P. On the kinetics and thermodynamics of excitons at the surface of semiconductor nanocrystals: are there surface excitons? *Chem. Phys.* **446**, 92–107 (2015).
10. Mittleman, D. M. et al. Quantum size dependence of femtosecond electronic dephasing and vibrational dynamics in CdSe nanocrystals. *Phys. Rev. B* **49**, 14435–14447 (1994).
11. Pham, P. V. et al. 2D heterostructures for ubiquitous electronics and optoelectronics: principles, opportunities, and challenges. *Chem. Rev.* **122**, 6514–6613 (2022).
12. Cao, Y. et al. Unconventional superconductivity in magic-angle graphene superlattices. *Nature* **556**, 43–50 (2018).
13. Ratchford, D. C. et al. Controlling the infrared dielectric function through atomic-scale heterostructures. *ACS Nano* **13**, 6730–6741 (2019).
14. Paudel, T. R. & Lambrecht, W. R. L. Computational study of phonon modes in short-period AlN/GaN superlattices. *Phys. Rev. B* **80**, 104202 (2009).
15. Hoglund, E. R. et al. Emergent interface vibrational structure of oxide superlattices. *Nature* **601**, 556–561 (2022).
16. Domínguez, C. et al. Length scales of interfacial coupling between metal and insulator phases in oxides. *Nat. Mater.* **19**, 1182–1187 (2020).
17. Middey, S. et al. Epitaxial strain modulated electronic properties of interface controlled nickelate superlattices. *Phys. Rev. B* **98**, 045115 (2018).
18. Frey, H., Beck, A., Huang, X., van Bokhoven, J. A. & Willinger, M. G. Dynamic interplay between metal nanoparticles and oxide support under redox conditions. *Science* **376**, 982–987 (2022).
19. He, J., Borisevich, A., Kalinin, S. V., Pennycook, S. J. & Pantelides, S. T. Control of octahedral tilts and magnetic properties of perovskite oxide heterostructures by substrate symmetry. *Phys. Rev. Lett.* **105**, 227203 (2010).
20. Tai, K., Lawrence, A., Harmer, M. P. & Dillon, S. J. Misorientation dependence of Al_2O_3 grain boundary thermal resistance. *Appl. Phys. Lett.* **102**, 034101 (2013).
21. Li, H. et al. Imaging moiré flat bands in three-dimensional reconstructed WSe_2/WS_2 superlattices. *Nat. Mater.* **20**, 945–950 (2021).
22. Lin, X., Liu, D. & Tománek, D. Shear instability in twisted bilayer graphene. *Phys. Rev. B* **98**, 195432 (2018).
23. Alden, J. S. et al. Strain solitons and topological defects in bilayer graphene. *Proc. Natl. Acad. Sci. USA* **110**, 11256–11260 (2013).
24. Yoo, H. et al. Atomic and electronic reconstruction at the van der Waals interface in twisted bilayer graphene. *Nat. Mater.* **18**, 448–453 (2019).
25. Jiang, L. et al. Soliton-dependent plasmon reflection at bilayer graphene domain walls. *Nat. Mater.* **15**, 840–844 (2016).
26. Susarla, S. et al. Hyperspectral imaging of exciton confinement within a moiré unit cell with a subnanometer electron probe. *Science* **378**, 1235–1239 (2022).
27. Eliel, G. S. N. et al. Intralayer and interlayer electron–phonon interactions in twisted graphene heterostructures. *Nat. Commun.* **9**, 1221 (2018).
28. Jorio, A. & Cançado, L. G. Raman spectroscopy of twisted bilayer graphene. *Solid State Commun.* **175-176**, 3–12 (2013).
29. Zhang, Z. et al. Engineering correlated insulators in bilayer graphene with a remote Coulomb superlattice. *Nat. Mater.* **23**, 189–195 (2024).
30. Lu, Z. et al. Fractional quantum anomalous Hall effect in multilayer graphene. *Nature* **626**, 759–764 (2024).
31. Uri, A. et al. Superconductivity and strong interactions in a tunable moiré quasicrystal. *Nature* **620**, 762–767 (2023).
32. Kang, K. et al. Evidence of the fractional quantum spin Hall effect in moiré $MoTe_2$. *Nature* **628**, 522–526 (2024).
33. Xiong, R. et al. Correlated insulator of excitons in WSe_2/WS_2 moire superlattices. *Science* **380**, 860–864 (2023).
34. Liu, E. et al. Excitonic and valley-polarization signatures of fractional correlated electronic phases in a WSe_2/WS_2 Moiré Superlattice. *Phys. Rev. Lett.* **127**, 037402 (2021).

35. Li, T. et al. Quantum anomalous hall effect from intertwined moiré bands. *Nature* **600**, 641–646 (2021).
36. Huang, X. et al. Correlated insulating states at fractional fillings of the WS₂/WSe₂ moiré lattice. *Nat. Phys.* **17**, 715–719 (2021).
37. Laussy, F. P., Kavokin, A. V. & Shelykh, I. A. Exciton-polariton mediated superconductivity. *Phys. Rev. Lett.* **104**, 106402 (2010).
38. Rogée, L. et al. Ferroelectricity in untwisted heterobilayers of transition metal dichalcogenides. *Science* **376**, 973–978 (2022).
39. Eberhard, B. Phonon spectroscopy by inelastic x-ray scattering. *Rep. Prog. Phys.* **63**, 171 (2000).
40. Gadre, C. A. et al. Nanoscale imaging of phonon dynamics by electron microscopy. *Nature* **606**, 292–297 (2022).
41. Szeftel, J. Surface phonon dispersion, using electron energy loss spectroscopy. *Surf. Sci.* **152-153**, 797–810 (1985).
42. Ripin, A. et al. Tunable phononic coupling in excitonic quantum emitters. *Nat. Nanotechnol.* **18**, 1020–1026 (2023).
43. Schmitt, D. et al. Formation of moiré interlayer excitons in space and time. *Nature* **608**, 499–503 (2022).
44. Johnson, R. C. Angular momentum on a lattice. *Phys. Lett. B* **114**, 147–151 (1982).
45. Zhang, L. & Niu, Q. Chiral phonons at high-symmetry points in monolayer hexagonal lattices. *Phys. Rev. Lett.* **115**, 115502 (2015).
46. Yoon, Y. et al. Terahertz phonon engineering with van der Waals heterostructures. *Nature* **631**, 771–776 (2024).
47. Chen, C. et al. Strong electron–phonon coupling in magic-angle twisted bilayer graphene. *Nature* **636**, 342–347 (2024).
48. Xu, Y. et al. Catalog of topological phonon materials. *Science* **384**, eadf8458 (2024).
49. Chen, L., Boulanger, M. E., Wang, Z. C., Tafti, F. & Taillefer, L. Large phonon thermal Hall conductivity in the antiferromagnetic insulator Cu₃TeO₆. *Proc. Natl. Acad. Sci. USA* **119**, e2208016119 (2022).
50. Jotzu, G. et al. Experimental realization of the topological Haldane model with ultracold fermions. *Nature* **515**, 237–240 (2014).
51. Thingstad, E., Kamra, A., Brataas, A. & Sudbø, A. Chiral phonon transport induced by topological magnons. *Phys. Rev. Lett.* **122**, 107201 (2019).
52. Pimenta Martins, L. G. et al. Pressure tuning of minibands in MoS₂/WSe₂ heterostructures revealed by moiré phonons. *Nat. Nanotechnol.* **18**, 1147–1153 (2023).
53. Lui, C. H. et al. Observation of interlayer phonon modes in van der Waals heterostructures. *Phys. Rev. B* **91**, 165403 (2015).
54. Li, Y. et al. Tuning commensurability in twisted van der Waals bilayers. *Nature* **625**, 494–499 (2024).
55. Hu, C., Naik, M. H., Chan, Y.-H. & Louie, S. G. Excitonic interactions and mechanism for ultrafast interlayer photoexcited response in van der waals heterostructures. *Phys. Rev. Lett.* **131**, 236904 (2023).
56. Sun, X. et al. Enhanced interactions of interlayer excitons in free-standing heterobilayers. *Nature* **610**, 478–484 (2022).
57. Loudon, R. J. The Raman effect in crystals. *Adv. Phys.* **13**, 423–482 (1964).
58. Zhu, H. et al. Observation of chiral phonons. *Science* **359**, 579–582 (2018).
59. Yankowitz, M. et al. Emergence of superlattice Dirac points in graphene on hexagonal boron nitride. *Nat. Phys.* **8**, 382–386 (2012).
60. Baek, J.-H. et al. Thermally induced atomic reconstruction into fully commensurate structures of transition metal dichalcogenide layers. *Nat. Mater.* **22**, 1463–1469 (2023).
61. van der Zande, A. M. et al. Tailoring the electronic structure in bilayer molybdenum disulfide via interlayer twist. *Nano Lett.* **14**, 3869–3875 (2014).
62. Mohiuddin, T. M. G. et al. Uniaxial strain in graphene by Raman spectroscopy: G peak splitting, Gruneisen parameters, and sample orientation. *Phys. Rev. B* **79**, 205433 (2009).
63. Dadgar, A. M. et al. Strain engineering and Raman Spectroscopy of monolayer transition metal dichalcogenides. *Chem. Mater.* **30**, 5148–5155 (2018).
64. Naik, M. H. et al. Intralayer charge-transfer moiré excitons in van der Waals superlattices. *Nature* **609**, 52–57 (2022).
65. Gadelha, A. C. et al. Localization of lattice dynamics in low-angle twisted bilayer graphene. *Nature* **590**, 405–409 (2021).
66. Kennes, D. M. et al. Moiré heterostructures as a condensed-matter quantum simulator. *Nat. Phys.* **17**, 155–163 (2021).
67. Alexeev, E. M. et al. Resonantly hybridized excitons in moiré superlattices in van der Waals heterostructures. *Nature* **567**, 81–86 (2019).
68. Paradisanos, I. et al. Controlling interlayer excitons in MoS₂ layers grown by chemical vapor deposition. *Nat. Commun.* **11**, 2391 (2020).
69. Giannozzi, P. et al. QUANTUM ESPRESSO: a modular and open-source software project for quantum simulations of materials. *J. Phys. Condens. Matter* **21**, 395502 (2009).
70. Togo, A. & Tanaka, I. First principles phonon calculations in materials science. *Scr. Mater.* **108**, 1–5 (2015).

Author contributions

L.L., L.Z., and C.C. conceived and designed the project. L.L. and J.C. fabricated samples and performed optical measurements. L.L. analyzed the experimental data and performed density-functional theory calculations. L.L., L.Z., and C.C. co-wrote the manuscript with input from all co-authors. L.L., J.C., L.H., Z.Q., Z.Z., R.L., L.Z., and C.C. discussed the results, data analysis and the paper.

Competing interests

The authors declare no competing interests.

Additional information

Supplementary information The online version contains supplementary material available at https://doi.org/10.1038/s41467-025-59325-w.

Correspondence and requests for materials should be addressed to Lijia Li, Lirong Zheng or Chunxiao Cong.

Peer review information *Nature Communications* thanks Eric Hoglund and the other, anonymous, reviewer(s) for their contribution to the peer review of this work. A peer review file is available.

Reprints and permissions information is available at http://www.nature.com/reprints